Radiofrequency-Triggered Tumor-Targeting Delivery System for Theranostics Application
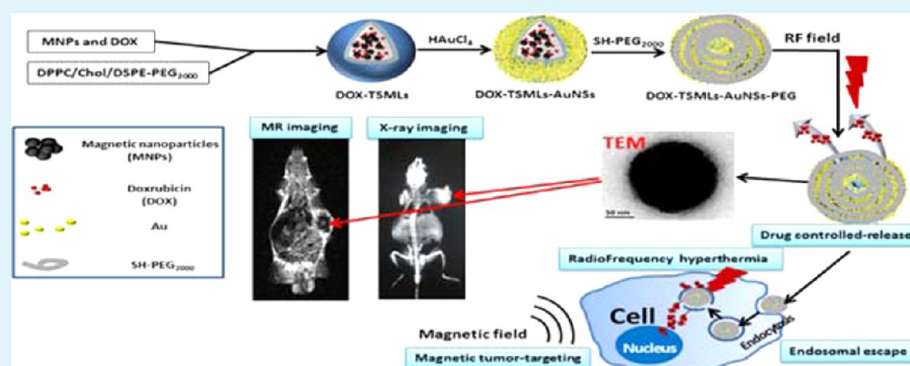
Lei Wang,[†,‡] Panpan Zhang,[‡] Jinjin Shi,[‡] Yongwei Hao,[‡] Dehui Meng,[‡] Yalin Zhao,[‡] Yin Yanyan,[§] Dong Li,[‡] Junbiao Chang,*[†] and Zhenzhong Zhang*[‡]

[†]School of Chemistry and Molecular Engineering, [‡]School of Pharmaceutical Sciences, and [§]School of Public Health, Zhengzhou University, 100 Kexue Avenue, Zhengzhou 450001, PR China

ABSTRACT: In this study, a new type of magnetic tumor-targeting PEGylated gold nanoshell drug delivery system (DOX-TSMLs-AuNSs-PEG) based on doxorubicin-loaded thermosensitive magnetoliposomes was successfully obtained. The reverse-phase evaporation method was used to construct the magnetoliposomes, and then gold nanoshells were coated on the surface of it. The DOX-TSMLs-AuNSs-PEG delivery system was synthesized after SH-PEG$_{2000}$ modification. This multifunction system was combined with a variety of functions, such as radiofrequency-triggered release, chemo-hyperthermia therapy, and dual-mode magnetic resonance/X-ray imaging. Importantly, the DOX-TSMLs-AuNSs-PEG complex was found to escape from endosomes after cellular uptake by radiofrequency-induced endosome disruption before lysosomal degradation. All results *in vitro* and *in vivo* indicated that DOX-TSMLs-AuNSs-PEG is a promising effective drug delivery system for diagnosis and treatment of tumors.

KEYWORDS: *thermosensitive magnetoliposomes, gold nanoshells, dual-mode MR/X-ray imaging, controlled release, chemo-hyperthermia therapy*

1. INTRODUCTION

With the development of nanotechnology, research in drug delivery systems has a new pace and dimension. An important challenge is to design an all-in-one drug delivery system that can be used for multiple purposes, including tumor targeting therapy, NIR-, light-, or pH-induced controlled release, photothermal therapy (PTT), photodynamic therapy (PDT), and diagnosis.[1−4] Generally, the disadvantages of drug delivery systems are toxicity, nontargeted, spanking release, and prolonged retention in the physiological system. Therefore, we have developed one type of intelligent drug delivery system based on gold-coated thermosensitive magnetoliposomes (TSMLs) to solve these problems.

In conventional chemotherapy, intravenous administration of drugs leads to their accumulation in both tumor sites and normal tissues and limits its success due to severe side effects.[5,6] Significant progress has been made in reducing the acute toxicity of drugs by application of liposomal formulations. For example, a liposome-based doxorubicin (DOX) formulation (Caelyx, Schering-Plough; DOXIL, OrthoBiotech) is approved for clinical use in cancer therapy and outperforms the free DOX

in therapeutic index.[7,8] It has been found that sterically stabilized liposomes can accumulate significantly in tumors by the enhanced permeability and retention (EPR) effect.[9] The therapeutic effects of liposomal formulations can be enhanced by tumor targeting and by triggering drug release within the tumors.

Recently, TSMLs have attracted much attention. Magnetic nanoparticles (MNPs) based on iron oxide (Fe_3O_4) are known for their immense potential in the field of magnetic field-based tumor targeting and cancer theranostics.[10−12] TSMLs appear to be a versatile delivery system due to biocompatibility, chemical functionality, and their potential for drug delivery.[13,14] Moreover, both MNPs and TSMLs can be used as a T_2 (spin−spin relaxation) contrast agent for magnetic resonance imaging (MRI), and thus their biodistribution can be monitored *in vivo* noninvasively by MRI.[15]
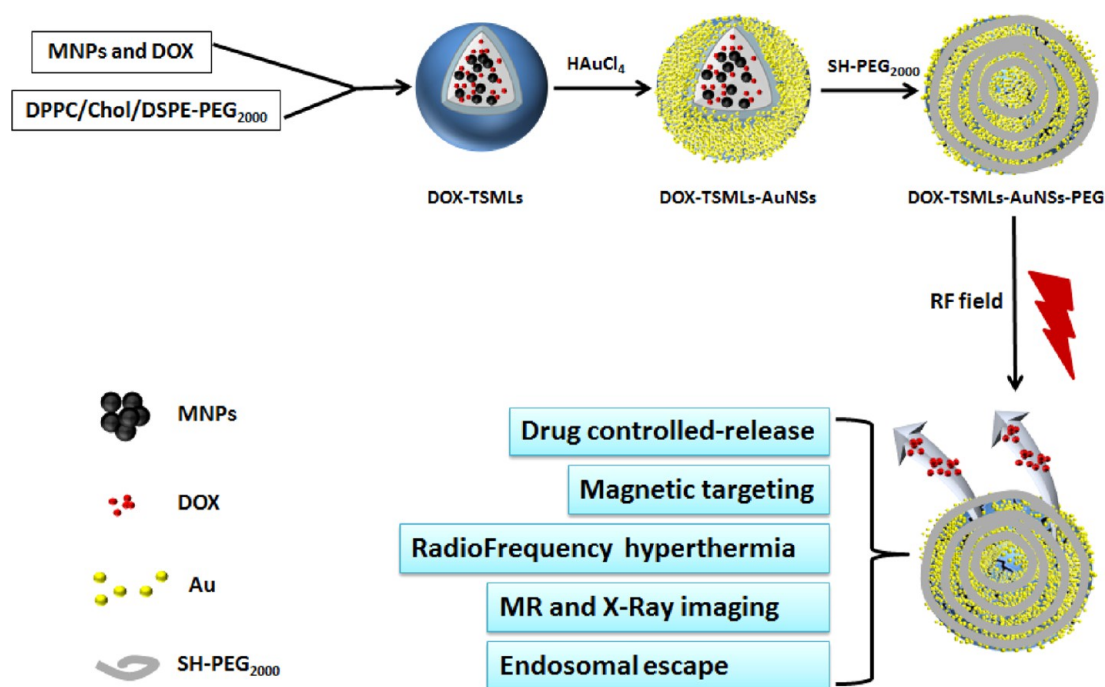
Figure 1. Scheme of DOX-TSMLs-AuNSs.

Thermosensitive liposomes (TSLs) have a long history of development as carriers of agents for triggered release and continue to be actively investigated. The metastable character of liposomes allows for applications in which leakage can be attained in response to specific stimuli, including pH,[16,17] enzymatic activity,[18] ultrasound,[19] and temperature.[20] The thermosensitive controlled release is associated with increased permeability of lipid membranes at their phase-transition temperatures. However, in clinical applications, local modulation of temperature-triggered release is often difficult to achieve. To do this, gold nanoshells (AuNSs) were used as a thermosensitive agent to induce the decomposition of TSLs in this study.

Gold nanomaterials have been widely used in the treatment of cancer which had attracted greater attention from researchers because it was demonstrated that gold nanomaterial structures have great potential for cancer PTT. Gold nanostructures, including nanoshells,[21,22] nanorods,[23] nanocages,[24] etc., have a strong surface plasmon resonance (SPR) in the near-infrared (NIR) region. This characteristic is good for cancer photothermal therapy because these gold nanostructures can be easily excited by NIR radiation.

Although the hyperthermia induced by NIR light can treat cancer, it has disadvantages that limit its practical implementation as a therapy. On one hand, noninvasive NIR heating is only effective at treating subsurface cancer (approximately a few millimeters deep) due to significant scattering and attenuation of NIR light by biological tissues.[25,26] On the other hand, the NIR light beams often focus on one site, which could cause damage to normal skin.[27] Therefore, the radiofrequency (RF) method was used to overcome the major limitations mentioned above. RF ablation is the most commonly used percutaneous ablation technique and is well-documented in the literature on focal therapies.[28] It has become the image-guided ablation method of choice because of its efficacy, safety, and ease of use. RF ablation has shown promise in treating selected solid tumors, particularly those involving the liver, kidneys, lungs, and pancreatic system.[29,30] It is a minimally invasive technique often used in inoperable patients with other comorbidities. Moreover, AuNSs deliver remarkable thermal power dissipation under capacitively coupled RF fields (13.56 MHz).[31]

Among all stimuli, RF provides a great opportunity to deliver a drug at the desired area in time, which is considered a key tool to amplify drug efficacy in cancer treatment with minimum adverse effects. Even with a specific delivery to cancer cells these types of drugs are taken up by means of endocytosis and are sequestered in endo-/lysosomal compartments where they are subjected to enzymatic degradation resulting in lack of biological effect.[32] Previous studies reported that NIR-induced photothermal could trigger disruption of the endo-/lysosomal membranes by photoinduced local heat generation.[33,34]

This paper aims to develop a type of PEGylated gold-coated TSML loaded with DOX for the diagnosis and treatment of cancer. First, the reverse-phase evaporation method was used to construct the TSMLs (DPPC:Chol:DSPE-PEG$_{2000}$ = 80:20:5 molar ratio), which enclose DOX (for chemotherapy) and MNPs (for tumor targeting and MR imaging). Then, gold seeds were coated on the surface of TSMLs and gradually formed AuNSs for DOX-triggered release by the RF field and X-ray CT imaging (Figure 1). Importantly, we also detected the mechanism of endosome escape (Figure 8).

2. EXPERIMENTAL SECTION

2.1. Materials. Doxorubicin (DOX, purity >98%) was received from Beijing Yi-He Biotech Co. Ltd. Phospholipids were purchased from Avanti Polar Lipids, USA. Sulforhodamine B (SRB), DMEM cell culture medium, penicillin, streptomycin, fetal bovine serum (FBS), and heparin sodium were bought from Gibco Invitrogen. FeCl$_3$·6H$_2$O, FeCl$_2$·4H$_2$O, HAuCl$_4$, and all the other chemicals were obtained from Sigma-Aldrich Co. LLC.

2.2. Preparation of MNPs. The magnetic nanoparticles were synthesized by the coprecipitation method. FeCl$_3$·6H$_2$O and FeCl$_2$·4H$_2$O (1.9:1 molar ratio) were dissolved in nitrogen-purged deionized water in a flask, and then the flask was filled with nitrogen gas and stirred in an oil bath (80 °C). Aqueous ammonia was slowly injected

into the mixture to adjust the pH value to 9−10 while stirring for 30 min. Citric acid dissolved in deionized water was then added to the solution. The temperature was raised to 95 °C, and the solution was stirred for another 90 min. The final mixture was cooled to room temperature, and then particles were magnetically separated from the supernatant. Then the magnetic nanoparticles were washed with distilled water until the pH value descended to 7.0.

2.3. Preparation of DOX-TSMLs. TSMLs were prepared by the reverse-phase evaporation method. Briefly, the mixture of DPPC:Chol:DSPE-PEG$_{2000}$ (80:20:5 molar ratio) was dissolved in a solution of chloroform−methanol (2:1 v/v) and then emulsified by sonication with a solution containing 10 mg of MNPs and 5 mg of DOX for 1 h in a bath sonicator. The organic solvent was evaporated by a rotary evaporator under reduced pressure until a homogeneous dispersion was formed. DOX-TSMLs and unencapsulated MNPs were collected by a permanent magnet, and the suspension was then centrifuged at 4000 rpm for 15 min to remove unencapsulated MNPs and retained DOX-TSMLs in the supernatant. The samples were stored at 4 °C until further characterizations.

2.4. Preparation of PEGylated DOX-TSMLs-AuNSs. In order to reduce gold nanoparticles (AuNPs) onto the surface of DOX-TSMLs, the HAuCl$_4$ aqueous solution (100 mM) was added to the previously prepared DOX-TSML complex solution under gentle swirling for uniform distribution. Then, the ascorbic acid solution (0.5 M) was added under gentle swirling for 1, 2, and 5 min, respectively. Following reduction, the gold-coated liposomes were dialyzed twice against deionized water at 4 °C. Finally, SH-PEG$_{2000}$ was immediately added into the solution with a gentle vortex, followed by magnetic collection to remove the unbound SH-PEG$_{2000}$ to obtain DOX-TSMLs-AuNSs-PEG. Au concentration was determined by the inductively coupled plasma mass spectrometry (ICP-MS, Varian Vista, Agilent Technologies) method.[35]

2.5. Characterization. DLS (Zetasizer Nano ZS-90, Malvern, UK), transmission electron microscopy (TEM, Tecnai G2 20, FEI), cryogenic transmission microscopy (Cryo-TEM, JEOL 2100 HC), and Fourier transform infrared (FT-IR) spectra were used for characterizing particle size, zeta potential, morphology, and functionalization of DOX-TSMLs-AuNSs-PEG complexes, respectively. The crystallinity of the synthesized nanoparticles was evaluated using X-ray diffraction (XRD) equipment (model: XD-3X, Beijing, China) with a Cu Ka X-ray source (λ = 1.54056 Å). Energy-dispersive spectroscopy (EDS) analysis was performed using an adjacent Oxford INCA system. The optical properties of DOX-TSMLs-AuNSs-PEG were characterized using an UV−vis spectrometer (Lambda 35, PerkinElmer, USA). A vibrating sample magnetometer (VSM) was used for characterizing the magnetic property of DOX-TSMLs-AuNSs-PEG complexes. The in vitro and in vivo T$_2$-weighted MR images were conducted on a 3-T clinical MRI scanner (SIEMENS). The X-ray images were conducted on a clinical X-ray scanner (SIEMENS).

2.6. Drug Encapsulation Efficiency and RF-Triggered Release. In order to calculate the drug encapsulation efficiency, the DOX concentration of DOX-TSMLs was determined by a fluorescence spectrophotometer (Shimadzu, Japan, Ex: 479, Em: 545) upon addition of Triton X-100. The amount of encapsulated iron was determined based on the ferrous ion by using phenanthroline colorimetry as described in previous literature.[36] Encapsulation efficiency and drug loading content were then calculated by using following formula

$$\text{encapsulation efficiency (\%)} = \frac{\text{amount of DOX in liposomes}}{\text{initial amount of DOX}} \times 100\%$$

$$\text{drug loading content (\%)} = \frac{\text{amount of DOX in liposomes}}{\text{total amount of liposomes}} \times 100\%$$

The release of DOX from DOX-TSMLs was studied by dialyzing (molecular weight cutoff: 1000 Da) the liposomes in PBS (pH 7.4). The sample was treated with or without RF irradiation (13.56 MHz, 300 W) for different time (10, 20, 30, 40 min). The released free DOX was quantified by high performance liquid chromatography (HPLC) before and after irradiation. Samples were analyzed on a Waters

symmetry C18 column (4.6 × 150 mm, 5 μm): the mobile phase was the mixture of methanol and 10 mM potassium phosphate monobasic buffer (68:32, v/v), column temperature was maintained at 25 °C, and the fluorescence detector was operated at an excitation wavelength of 479 nm and an emission wavelength of 545 nm.

2.7. Cellular Experiments. *2.7.1. Cell Culture.* The HepG2 human liver cancer cell line was cultured in DMEM culture medium with 1% penicillin/streptomycin and 10% fetal bovine serum at 37 °C in a humidified incubator.

2.7.2. Cell Viability. HepG2 cells were seeded into 96-well plates, and after 24 h incubation, cells were treated with DOX and TSMLs-AuNSs-PEG for another 24 h to detect the cytotoxicity of the blank vector. HepG2 cell inhibition of DOX and DOX-TSMLs-AuNSs-PEG drug delivery systems was also detected. First, HepG2 cells were seeded into 96-well plates for 24 h. Second, cells were incubated with DOX and DOX-TSMLs-AuNSs-PEG for 2 h at different concentrations, and then fresh medium was added. After total 24 h incubation, cell viability was measured by the sulforhodamine B assay (SRB).

For magnetic targeting and RF irradiation experiments, the cell culture plates were positioned on a format magnetic plate. After 2 h treatment with DOX and DOX-TSMLs-AuNSs-PEG (DOX concentration: 1 μg/mL), cells were irradiated with RF (13.56 MHz, 300 W) for 10 min. After incubation (total 24 h), cell viability was measured by SRB.

2.7.3. Cellular Uptake and Magnetic Tumor Targeting. To detect intracellular DOX-TSMLs-AuNSs-PEG uptake characteristics, HepG2 cells were seeded on glass coverslips in six-well plates for 24 h prior to incubation at a density of 1 × 10^5/well with DOX-TSMLs-AuNSs-PEG (DOX concentration: 1 μg/mL) for 2 h with or without magnetic treatment. After washing with PBS, the cells were imaged by a CytoViva Hyperspectral Imaging System (HIS) (Olympus BX51). The percentage of DOX-TSMLs-AuNSs that are able to enter the cells was also detected by the ICP method. For detection of magnetic tumor targeting, propidium iodide (PI) was added. After 30 min incubation, cells were washed three times with PBS, and the fluorescence images were acquired using a fluorescence microscope (Zeiss LSM 510).

2.7.4. Endosomal Escape. To assess the effect of endosome escape of the DOX-TSMLs-AuNSs-PEG, cells were incubated the same as step 2.7.3 with the DOX-TSMLs-AuNSs-PEG complexes for 2 h with a magnet. After RF irradiation, the cells were imaged through a fluorescence microscope (Zeiss LSM510).

2.8. Animal Experiments. *2.8.1. Tumor-Bearing Mice Model.* All animal experiments were performed according to the national guidance and approved by the experiment animal ethical committee of Zhengzhou University. Male BALB/c mice (18−20 g) were purchased from the Henan laboratory animal center. S180 cells (2 × 10^6) suspended in 0.1 mL of saline were subcutaneously injected into the right shoulder of each mouse. About 6 days after tumor inoculation, the tumor volume reached about 100 mm^3, and the S180 tumor-bearing mice models were generated.

2.8.2. Tumor Treatment in Vivo. Tumor-bearing mice were divided into 10 groups (5 mice per group). The mice were intravenously injected via the tail vein with normal saline, DOX, TSMLs-AuNSs-PEG, and DOX-TSMLs-AuNSs-PEG (DOX concentration: 5 mg/kg, magnetic field intensity 0.4 T, RF condition: 13.56 MHz, 300 W, 10 min) every other day, named NS, DOX, TSMLs-AuNSs-PEG, TSMLs-AuNSs-PEG+Magnet, TSMLs-AuNSs-PEG+RF, TSMLs-AuNSs-PEG+Magnet+RF, DOX-TSMLs-AuNSs-PEG, DOX-TSMLs-AuNSs-PEG+RF, DOX-TSMLs-AuNSs-PEG+Magnet, and DOX-TSMLs-AuNSs-PEG+Magnet+RF, respectively. The RF groups were exposed to the RF field at 4 h postinjection. The mice were observed daily for clinical symptoms, and the tumor sizes were measured by a caliper every 2 day for 2 weeks. The tumor volume was calculated according to the following formula: width^2 × length/2.

After 14 days of treatment, the mice were killed to collect the heart, liver, spleen, lung, kidney, and tumor. These collected tissues were soaked into formalin solution and then embedded with paraffin for
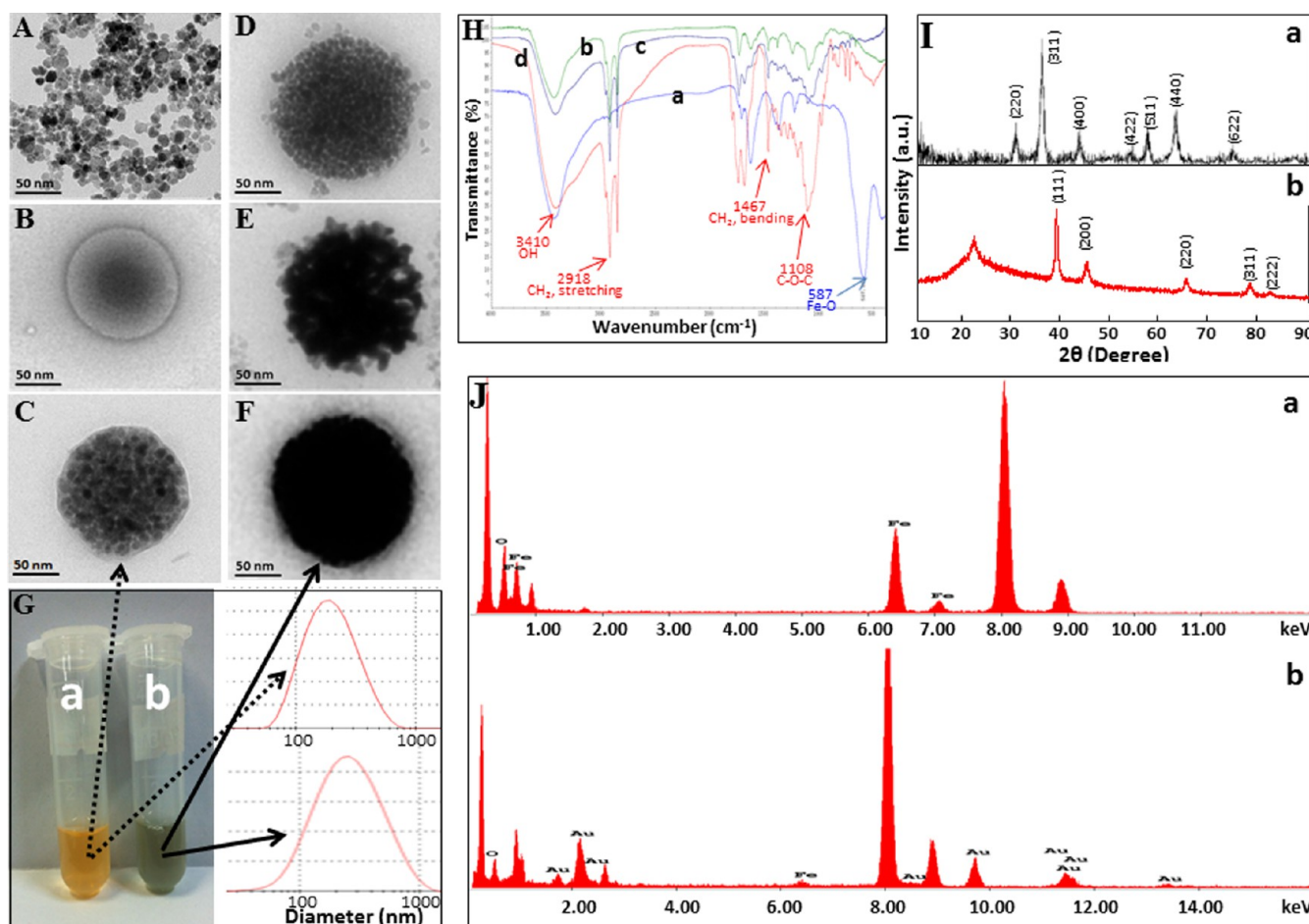
Figure 2. TEM images of (A) MNPs, (B) DOX-TSLs, (C) DOX-TSMLs, and (D ~ F) the constructed procedure of DOX-TSMLs-AuNSs-PEG with reduction time at 1, 2, and 5 min, respectively. (G) Photos and particle sizes of (a) DOX-TSLs and (b) DOX-TSMLs. (H) FT-IR spectra of (a) Fe_3O_4, (b) DOX-TSMLs, (c) DOX-TSMLs-AuNSs, and (d) DOX-TSMLs-AuNSs-PEG. (I) XRD patterns of (a) Fe_3O_4 and (b) DOX-TSMLs-AuNSs-PEG. (J) EDS analysis of (a) Fe_3O_4 and (b) DOX-TSMLs-AuNSs-PEG.

H&E stain. Morphological changes were observed under a microscope (ZeissLSM510).

2.8.3. Biodistribution Study of DOX. The tumor-bearing mice were divided into three groups (five mice per group), selecting one group to paste a magnet on the tumor site of each mouse. After fasted but water ad libitum for 12 h, the DOX, DOX-TSMLs-AuNSs-PEG (DOX concentration: 5 mg/kg), were injected by tail vein into the tumor-bearing mice, respectively. The magnet group was also injected with DOX-TSMLs-AuNSs-PEG complexes, named the DOX-TSMLs-AuNSs-PEG+Magnet group. After injection for 4 h, the mice were sacrificed to dedicate the heart, liver, spleen, lung, kidney, and tumor. After separation and extraction, the concentration of DOX in the samples was analyzed by HPLC use the same method described above.

2.8.4. MR Imaging and X-ray Imaging in Vivo. In order to investigate the imaging properties and diagnostic potential of DOX-TSMLs-AuNSs-PEG, the MR and X-ray imaging based on the characteristics of MNPs and AuNPs in DOX-TSMLs-AuNSs-PEG was detected.

For in vivo MR and X-ray imaging, DOX-TSMLs-AuNSs-PEG (200 μL; DOX concentration: 5 mg/kg; Fe concentration: ~7.5 mM) were intravenously injected into the tumor-bearing mice. After injection for 4 h, MR and X-ray imaging were conducted on a clinical 3-T MRI scanner and X-ray scanner, respectively.

2.9. Statistical Analysis. Quantitative data were expressed as Mean ± SD and analyzed by analysis of variance (ANOVA) followed by Dunnett post test. *P* values <0.05 were considered statistically significant.

3. RESULTS AND DISCUSSION

The first liposomal pharmaceutical product, Doxil (Ben Venue Laboratories, Inc., Bedford, OH), received US Food and Drug Administration (FDA) approval in 1995, and colloidal gold already has FDA approval for treatment of arthritis by internal administration. Given that some considerable effort is being expended toward establishing a drug delivery system for liposomes and GNPs in cancer therapy. A holy grail in cancer therapy is to deliver a high dose of drug to tumor sites for maximum treatment efficacy while minimizing side effects to normal organs. For these purposes, a PEGylated tumor-targeting radio-frequency-triggered drug delivery system based on thermosensitive magnetoliposomes (DOX-TSMLs-AuNSs-PEG) was constructed. The protocol for preparation of DOX-TSMLs-AuNSs-PEG is shown in Figure 1.

3.1. Preparation and Characterization of DOX-TSMLs-AuNSs-PEG. DOX-TSMLs-AuNSs-PEG (DPPC:Chol:DSPE-PEG_{2000} = 80:20:5 molar ratio) enclosing DOX and MNPs in the inner phase were prepared by the reverse-phase evaporation method followed by coating with AuNSs and connecting with SH-PEG_{2000} through the S−Au bond. As shown in Figure 2A, TEM images of MNPs showed a uniform size in the range of 12−15 nm, which is desired for the particles to be superparamagnetic in nature. The size and morphology of DOX-TSLs, DOX-TSMLs, and DOX-TSMLs-AuNSs-PEG
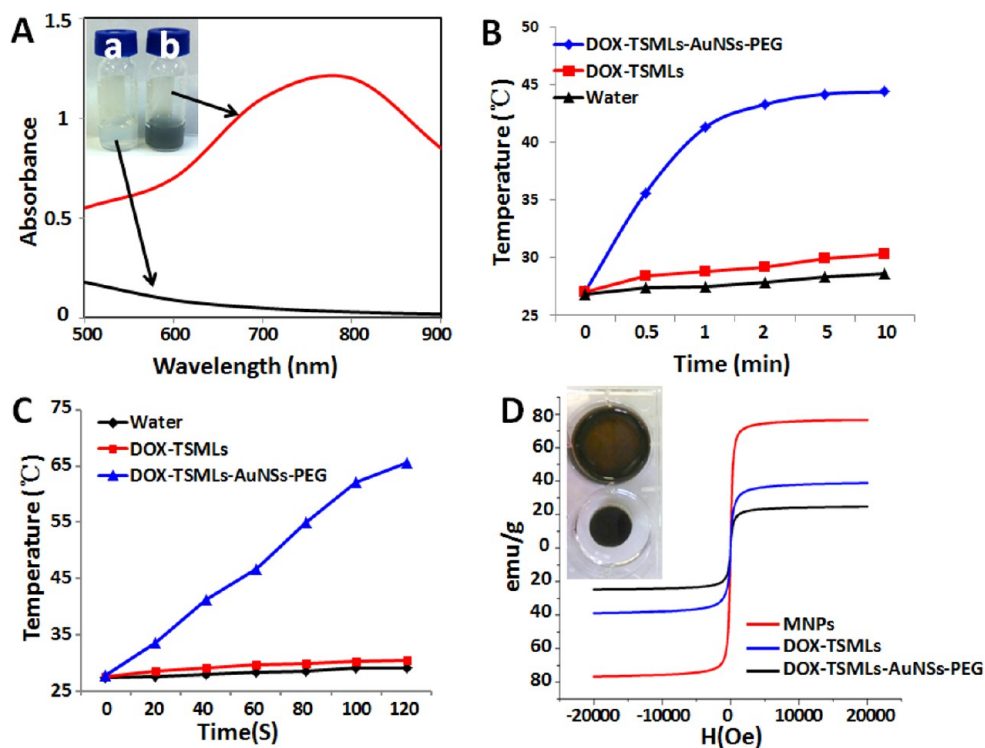
Figure 3. (A) UV−vis spectrogram of TSLs-AuNSs-PEG and TSLs; (B) 13.56 MHz RF irradiation at 300 W; (C) temperature evolution of water, DOX-TSMLs, and DOX-TSMLs-AuNSs-PEG under 808 nm NIR laser irradiation at 1.4 W/cm^2; (D) magnetization loops of MNPs, DOX-TSMLs, and DOX-TSMLs-AuNSs-PEG.

were confirmed by cryo-TEM. TSLs-DOX clearly had a spherical shape (Figure 2B), and magnetic particles were densely packed within the DOX-TSMLs (Figure 2C). The HAuCl$_4$ was, therefore, reduced by the ascorbic acid on the surface of DOX-TSMLs. However, AuNPs or AuNSs on the surface of DOX-TSMLs were not stable, so SH-PEG$_{2000}$ was used to solve this problem further for prolonging the circulation of them *in vivo*. After gold seeds were reduced initially, we could clearly see that AuNPs were coated on the surface of DOX-TSMLs (Figure 2D). With the increase of reduction time, a lot of AuNPs gradually got together, indicating that the color would deepen when a lot of AuNPs are connected or overlaid with each other (Figure 2E). Finally, AuNPs gradually formed shells. The structures of the DOX-TSMLs-AuNSs-PEG were difficult to observe (Figure 2D), indicating that the DOX-TSMLs were successfully coated with AuNSs. The size and morphology of DOX-TSMLs and DOX-TSMLs-AuNSs-PEG were also confirmed by DLS. The average size of DOX-TSMLs was 184.8 ± 1.2 nm and DOX-TSMLs-AuNSs-PEG was 208.3 ± 1.3 nm (Figure 2C).

Figure 2H displayed the FT-IR spectrum of Fe$_3$O$_4$, DOX-TSMLs, DOX-TSMLs-AuNSs, and DOX-TSMLs-AuNSs-PEG. The spectra of the Fe$_3$O$_4$ (Figure 2H-a) showed a broad strong band at ∼587 cm^{-1} due to the Fe−O lattice mode of Fe$_3$O$_4$.[37] In Figure 2H-b and -c, the bands at ∼1245 cm^{-1} (the C−H bending) are the characteristic absorption of the P=O bond which was introduced by the liposomes (DPPC/Chol/DSPE-PEG$_{2000}$). DOX-TSMLs-AuNSs showed a new band induced by the ascorbic acid around 1685 cm^{-1}, while the band around 3430 cm^{-1} shifted to 3418 cm^{-1}, implying the involvement of the O−H groups in the reduction of Au ions.[38] Compared to DOX-TSMLs-AuNSs, the PEG coating was confirmed by the violent bands at ∼2918, ∼1467, and ∼1108 cm^{-1} correspond-

ing to the C−H stretching, the C−H bending, and the C−O stretching vibrations, respectively (Figure 2H-d), suggesting that the DOX-TSMLs-AuNSs-PEG drug delivery system was successfully constructed.

XRD patterns of Fe$_3$O$_4$ (a) and DOX-TSMLs-AuNSs-PEG (b) are shown in Figure 2I, and the six strong peaks in Figure 2I-a correspond to the (220), (311), (400), (422), (511), and (440) lattice planes of Fe$_3$O$_4$ (JCPDS No. 88-0315). In addition, the elemental mapping of Fe$_3$O$_4$ in Figure 2J-a proved that the product contains the element of oxygen (O) and iron (Fe). This result combined with the result of XRD indicated that Fe$_3$O$_4$ was successfully synthesized. After the AuNSs were reduced onto the surface of DOX-TSMLs, the diffraction peaks of Fe$_3$O$_4$ crystals in Figure 2I-b were not obvious; however, five new peaks which can be attributed to the crystal planes of (111), (200), (220), (311), and (222) of the face-centered cubic structure (FCC) of Au (JCPDS No. 65-8601) appeared,[39] demonstrating that the AuNSs have been successfully synthesized for wrapping the TSMLs. Moreover, the broad band presented at around $2\theta = 20°$ pointing to the organic amorphous peaks, and the peak that appeared at around 21° is the typical gel phase pattern for DPPC indicating the existence of liposomes without the AuNS shell.[40] After AuNSs had been constructed, the EDS spectrum of the DOX-TSMLs-AuNSs-PEG showed that the signal intensity corresponding to Fe almost disappeared, and new strong signals of Au appeared. This result combined with the TEM images shown in Figure 2A∼F indicated that the TSMLs were coated with AuNSs.

As seen in the UV−vis spectrum of TSLs-AuNSs-PEG, a broad absorption band between 500 and 900 nm was observed, which had a maximum at ∼800 nm (Figure 3A). The ability of AuNSs to convert light energy into heat was tested by using water as the heating medium. The temperature changes of
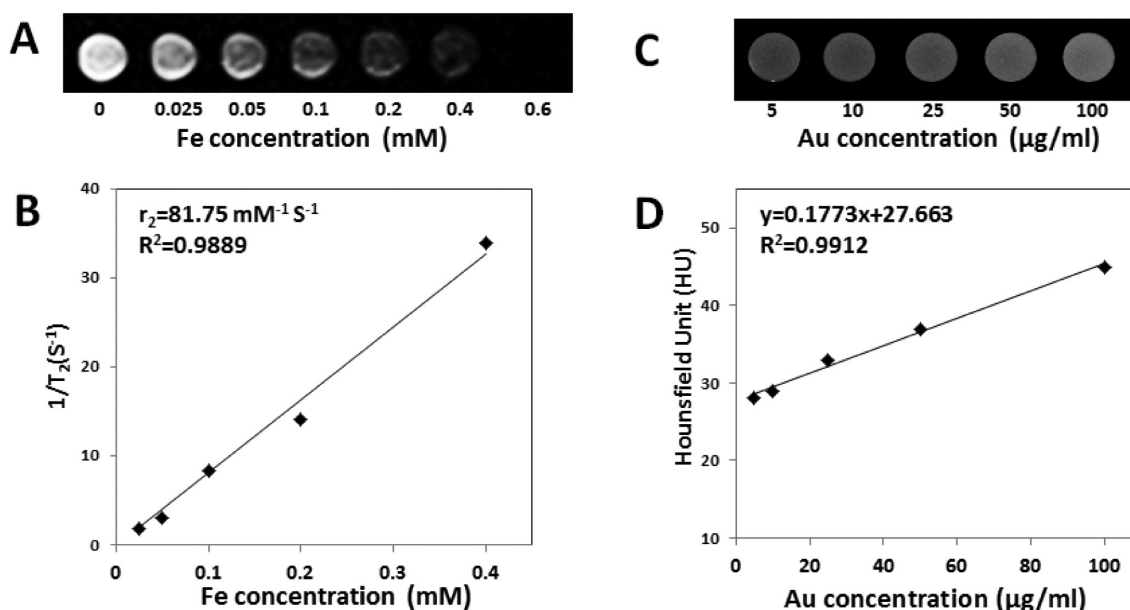
Figure 4. (A) T_2-weighted MR images of DOX-TSMLs-AuNSs-PEG solutions at different Fe concentrations. (B) T_2 relaxation rate R_2 ($1/T_2$) against Fe concentration. (C) *In vitro* X-ray CT images of DOX-TSMLs-AuNSs-PEG suspended in PBS. The Au concentration (μg/mL) in each sample is provided at the bottom of the respective images. (D) CT attenuation (HU) plot of DOX-TSMLs-AuNSs-PEG at various concentrations.

DOX-TSMLs-AuNSs-PEG were measured under RF irradiation (13.56 MHz, 300 W) (Figure 3B). The heating efficiency of DOX-TSMLs-AuNSs-PEG relies strongly on irradiation time; however, when the temperature reached about 45 °C, it no longer rose. This can be explained by the structures of TSMLs and AuNSs being destroyed when the temperature reached the phase-transition temperature of liposomes. DOX-TSMLs-AuNSs-PEG also displayed a marked sustained temperature increase within 2 min upon the 808 nm NIR laser irradiation (Figure 3C). Although TSMLs and AuNSs were destroyed, the other forms of gold nanomorphology were existent. We believe that both AuNSs and many other forms of AuNPs can lead to temperature elevation under 808 nm NIR light. However, photothermal therapy under NIR light frequently used in biomedical applications has limited penetration through and may cause damage to biological samples. Here, the RF hyperthermia method was used to overcome the limitations.

The magnetic properties of the DOX-TSMLs-AuNSs-PEG delivery system were characterized by a vibrating sample magnetometer. As shown in Figure 3D, the room-temperature magnetization curves of DOX-TSMLs and DOX-TSMLs-AuNSs-PEG had typical superparamagnetic behavior (49.7 and 35.8 emu/g). The saturation magnetization (Ms) of DOX-TSMLs-AuNSs-PEG was much less than that of MNPs (78.4 emu/g), which was attributed to liposomes, AuNSs, and PEG$_{2000}$.

MNPs have been widely used as T_2-contrast agents in MRI. Owing to the presence of MNPs inside DOX-TSMLs-AuNSs-PEG, the delivery system could act as a T_2 contrast agent for MRI. T_2-weighted MR imaging (Figure 4A) of DOX-TSMLs-AuNSs-PE solutions acquired on a 3-T MRI scanner revealed the concentration-dependent darkening effect. The transverse relaxivity (r_2) of DOX-TSMLs-AuNSs-PEG was 81.75 mM^{-1}·s^{-1} (Figure 4B). The dose-dependent MRI signal intensity displayed a significant MRI signal intensity decrease with the increase of the concentration of DOX-TSMLs-AuNSs-PEG, revealing the capability of DOX-TSMLs-AuNSs-PEG as an effective T_2 MRI contrast agent.

Recently, a number of nanoparticles or nanomaterials containing Au have been used for X-ray CT imaging.[41,42] In Figure 4C, as the concentration of Au increased, the CT signal intensity continuously increased, resulting in brighter images. In this study, the Hounsfield Units (HU) of DOX-TSMLs-AuNSs-PEG were investigated. These results suggest that DOX-TSMLs-AuNS-PEG has a potential application as a positive X-ray/CT imaging contrast agent. The previous reports showed that gold has a higher X-ray absorption coefficient than iodine (conventional CT contrast agents); therefore, it may be used to achieve the anticipated results in the body.[43]

3.2. Drug Encapsulation Efficiency and Release. The magnetic properties of TSMLs play an important role in magnetic tumor targeting and MR imaging. Thus, we adjusted the proportion of each component to make Fe content reach a maximum (~7.5 mM). Moreover, the DOX loading content and encapsulation efficiency were 12.85 ± 0.3% and 51.4 ± 0.6%.

To investigate the RF sensitivity of DOX-TSMLs-AuNSs-PEG as well as the release profile of DOX, the released drug with or without RF irradiation was measured. As shown in Figure 5A and 5B, the structure of DOX-TSMLs-AuNSs-PEG with RF irradiation was broken, and the Fe$_3$O$_4$ and DOX enclosed in TSMLs can be released quickly. Figure 5C showed that DOX release from DOX-TSMLs and DOX-TSMLs-AuNSs-PEG was quite slow without RF treatment at 37 °C. DOX release from DOX-TSMLs with RF irradiation was higher than without RF treatment, but the cumulative release was still very low, indicating that RF could promote the drug release from DOX-TSMLs, and this can be attributed to generation of very little heat of DOX-TSMLs under RF irradiation. However, when DOX-TSMLs-AuNSs-PEG was treated with RF irradiation, the drug release rate was increased rapidly. Moreover, the results showed that the DOX release rate was maintained at about 65% after 10 min under RF irradiation, indicating that the DOX-TSMLs-AuNSs-PEG complexes are stable at body temperature, but when exposed to RF field, AuNSs on DOX-
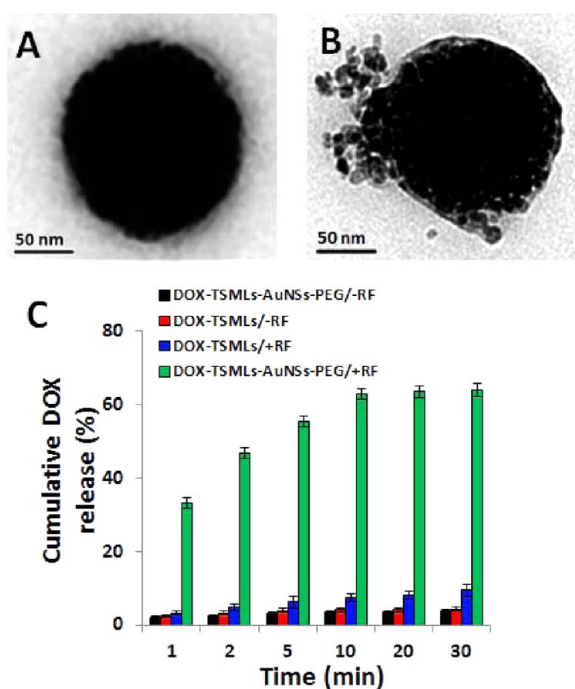
Figure 5. (A) TEM image of DOX-TSMLs-AuNSs-PEG. (B) TEM image of DOX-TSMLs-AuNSs-PEG with RF irradiation. (C) Cumulative DOX release of DOX-TSMLs and DOX-TSMLs-AuNSs-PEG with and without RF irradiation.
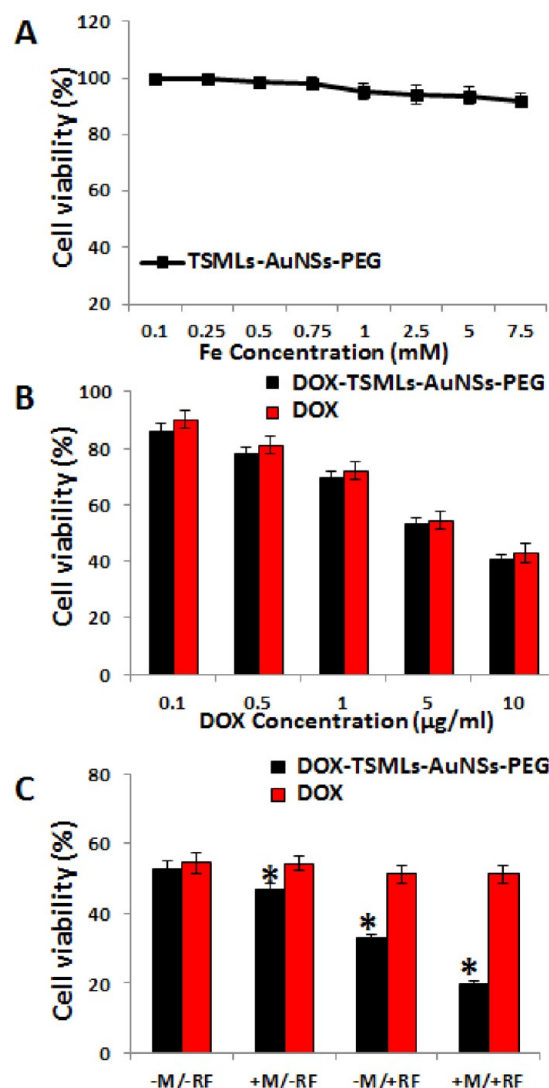

Figure 6. (A) Cytotoxicity of TSMLs-AuNSs-PEG. (B) The cytotoxicity of DOX and DOX-TSMLs-AuNSs-PEG at different concentration. (C) DOX and DOX-TSMLs-AuNSs-PEG (DOX concentration: 1 μg/mL) with a magnet and RF irradiation on HepG2 cells. (*) indicates a statistically significant difference compared with the DOX group (Mean ± SD, n = 3).

TSMLs can produce high temperature and cause drug-triggered release.

3.3. Cytotoxicity. The cytotoxicity of the blank vector on HepG2 cells was carried out at different concentrations as shown in Figure 6A. The results showed that the blank vector has no obvious toxicity on HepG2 cells. In Figure 6B, the cell viability of DOX and DOX-TSMLs-AuNSs-PEG was positively correlated with a dose at 24 h, and there was no significant difference among these groups at the different concentrations.

As shown in Figure 6C, the magnetic treatments have shown an apparent effect on the viability of HepG2 cells incubated with DOX-TSMLs-AuNSs-PEG complexes. This magnetic property could be utilized for magnetically enhanced drug delivery and caused higher cellular uptake of DOX. The results demonstrated that DOX-TSMLs-AuNSs-PEG has a strong magnetic tumor-targeting effect and hyperthermia effect under the RF field, and these properties could help to enhance DOX-TSMLs-AuNSs-PEG delivery into cells and improve the cell inhibition.

3.4. Cellular Uptake and Magnetic Targeting in Vitro. To explore the cellular uptake of DOX-TSMLs-AuNSs-PEG with or without magnetic targeting by HepG2 cells, we have tracked the delivery system internalization into the cells through colocalization of the Au signal (golden yellow fluorescence). Au was successfully identified in vitro through their spectral signature alone.[44] As shown in Figure 7A~C, HepG2 cells incubated with DOX-TSMLs-AuNSs-PEG for different periods of time clearly revealed the time-dependent cellular uptake manner. The fluorescence of the DOX-TSMLs-AuNSs-PEG group was enhanced after magnetic treatment (Figure 7D). After ICP detection, the calculated percentage of DOX-TSMLs-AuNSs in cells was 76.2 ± 3.1% and 89.3 ± 3.6% with or without magnetic treatment, respectively.

For further investigation of the magnetic targeting effect, HepG2 cells were incubated with DOX-TSMLs-AuNSs-PEG with a magnet (magnetic field intensity: 0.4 T) for 2 h (Figure 7E). After PI staining, there was only trace red fluorescence in cells outside the magnet, suggesting that only a small amount of cells died. At the edge of the magnet, red fluorescence has obvious demarcation, and cells above on the magnet showed strong fluorescence of PI in the whole vision, showing that a large amount of cells were killed in this position. All the results indicated that the DOX-TSMLs-AuNSs-PEG drug delivery system could be used for magnetic tumor-targeting application.

3.5. Endosome Escape. In order to make stronger the effect of drug delivery, the carrier systems with endosome escape effect are very favorable. The mechanism of RF hyperthermia induced endo-/lysosomal membrane disruption after cellular uptake was illustrated in Figure 8A. To further investigate the intracellular distribution behaviors of DOX, a high definition flourescence microscope was used to study the DOX-TSMLs-AuNSs-PEG complexes against HepG2 cells, and
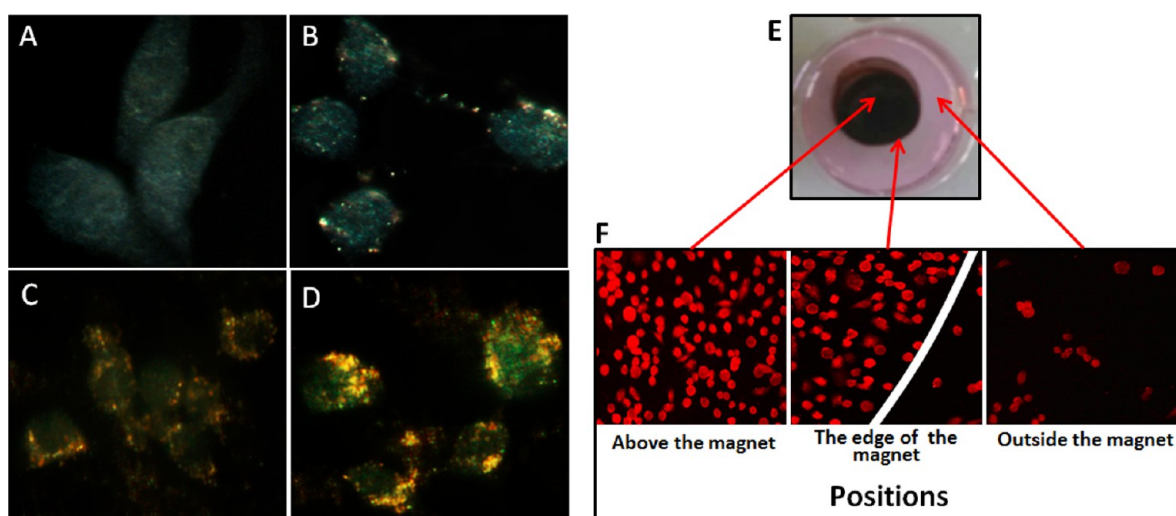
Figure 7. Dark-field image of the DOX-TSMLs-AuNSs-PEG nanoparticle-transfected HepG2 cells after incubation for 1 and 2 h with or without magnetic treatment. AuNSs: bright golden yellow color; cells: weak blue. (A) Blank cells; (B) cells + AuNSs 1 h; (C) cells + AuNSs 2 h; (D) cells + AuNSs + Magnet 2 h (400 ×). (E) Photo of the cell culture plate with a magnet (black color field) placed under it. (F) Fluorescence images of DOX-TSMLs-AuNSs-PEG treated HepG2 cells stained with PI (red, dead cells) in the presence of a magnet.
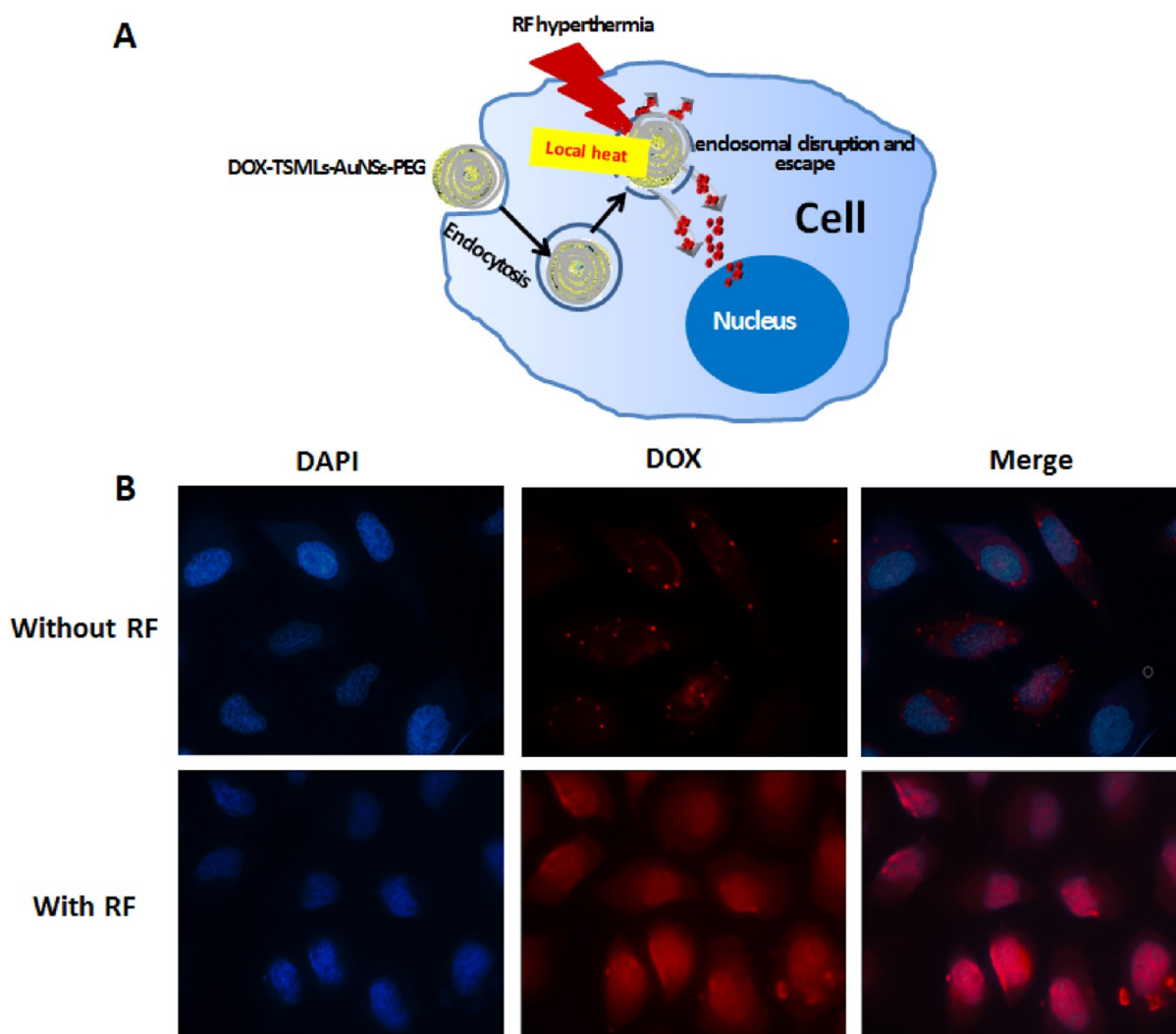

Figure 8. (A) Schematic illustration of the mechanism of cytosolic drug release by RF hyperthermia-induced endosome disruption and escape. (B) Fluorescence microscopy images of HepG2 cells incubated with DOX-TSMLs-AuNSs-PEG and treated with a magnet at 2 h with or without RF irradiation (400 ×).
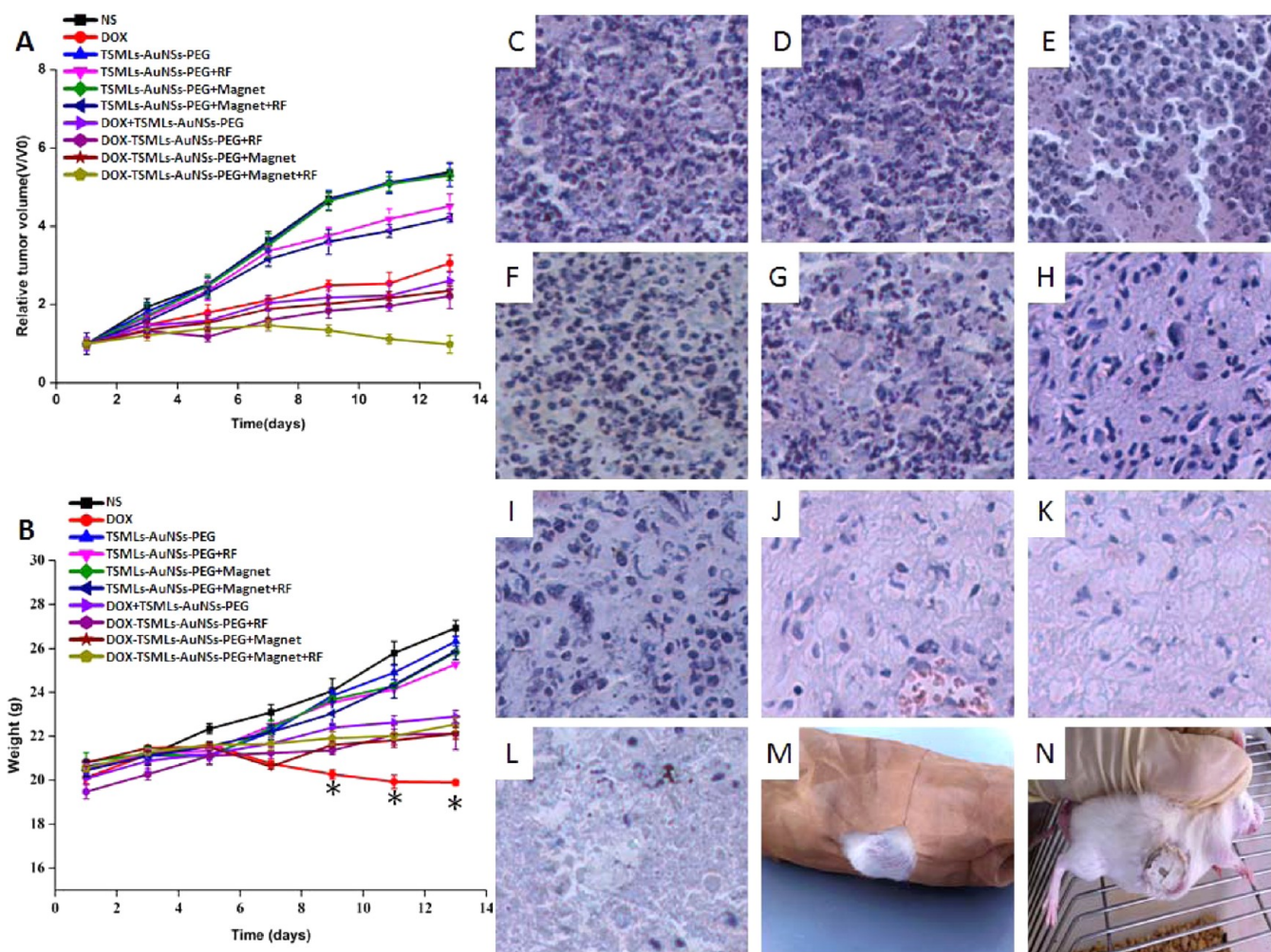
Figure 9. (A) Changes of relative tumor volume and (B) body weight of tumor-bearing mice in different groups during treatment (Mean ± SD, n = 6). Histologic assessments of tumor tissues with H&E staining (400 ×): (C) NS, (D) TSMLs-AuNSs-PEG, (E) TSMLs-AuNSs-PEG+RF, (F) TSMLs-AuNSs-PEG+Magnet, (G) TSMLs-AuNSs-PEG+Magnet+RF, (H) DOX, (I) DOX-TSMLs-AuNSs-PEG, (J) DOX-TSMLs-AuNSs-PEG+RF, (K) DOX-TSMLs-AuNSs-PEG+Magnet, and (L) DOX-TSMLs-AuNSs-PEG+Magnet+RF. Photos of (M) tumor-bearing mice after irradiation with RF (mice were wrapped with copper net, and the tumor sites were uncovered) and (N) tumor-bearing mice treated with a magnet.

the nuclei were labeled with DAPI. As shown in Figure 8B, DOX was concentrated as punctiform fluorescence in cells without RF irradiation, and we believe that the delivery system was in the endo-/lysosomes this time; however, the fluorescences were very weak due to the shield of AuNSs. After RF irradiation, the fluorescences in cells were significantly enhanced, and the fluorescence dots disappeared, indicating that the endo-/lysosomes were disrupted induced by RF hyperthermia and that DOX was released in cytoplasm for further delivery.

3.6. Tumor Growth Inhibition *in Vivo*. To investigate the *in vivo* therapeutic efficacy of DOX-TSMLs-AuNSs-PEG, comparative efficacy studies were conducted. The tumor-bearing mice were divided into 10 groups, and each group was treated according to the protocols described above. The changes of relative tumor volume were plotted in Figure 9A. Compared with the NS group, mice treated with TSMLs-AuNSs-PEG or TSMLs-AuNSs-PEG+Magnet showed little therapeutic effect. However, owing to the RF hyperthermia effect of AuNSs, the two groups with RF irradiation showed an obvious effect on tumor inhibition, suggesting that the blank carrier would not obviously inhibit the tumor growth and RF

that hyperthermia could inhibit the growth of the tumor. Compared with the control group and free DOX group, a tumor treated with DOX-TSMLs-AuNSs-PEG, DOX-TSMLs-AuNSs-PEG+Magnet, and DOX-TSMLs-AuNSs-PEG+Magnet+RF showed obvious inhibition, respectively, and there were significant differences among the three groups. These results demonstrated that this multifunctional delivery system has magnetic tumor-targeting, chemotherapy, and hyperthermia effects *in vivo*.

Allowing for high toxicity usually leads to weight loss, and the body weight of the tumor-bearing mice during the treatment were measured.[45,46] There was no weight loss observed in the groups treated with a delivery system (Figure 9B). However, the free DOX group appears to have a decrease in body weight. These results indicated that there was little toxicity of our drug delivery system *in vivo*, and this multifunctional nanolipsome can increase the therapeutic index of DOX.

The results of therapeutic efficacy and toxicity detected by H&E staining are shown in Figure 9C~L. The NS group showed vigorous growth, while the heteromorphosis to a certain extent occurred in tumor cells with cell necrosis, lysis, and fragment in the DOX, DOX-TSMLs-AuNSs-PEG, DOX-

TSMLs-AuNSs-PEG+RF, DOX-TSMLs-AuNSs-PEG+Magnet, and DOX-TSMLs-AuNSs-PEG+Magnet+RF groups. No significant morphological change was found in the TSMLs-AuNSs-PEG and TSMLs-AuNSs-PEG+Magnet groups, but in TSMLs-AuNSs-PEG+RF and TSMLs-AuNSs-PEG+Magnet +RF groups. A large amount of dead cells in tumor tissue was observed in the mice treated with DOX-TSMLs-AuNSs-PEG+Magnet+RF, indicating the great magnetic tumor-targeting and chemo-hyperthermia therapy effect in the tumor sites.

3.7. Biodistribution of DOX for the Drug Delivery System. Biodistribution is an important index to evaluate the drug delivery system for biological application. In order to learn the amount of DOX in different tissues and understand the tumor treatment efficacy of various DOX formulations, we investigated the biodistribution of free DOX, DOX-TSMLs-AuNSs-PEG, and DOX-TSMLs-AuNSs-PEG+Magnet, respectively. As shown in Figure 10, the differences were obvious after
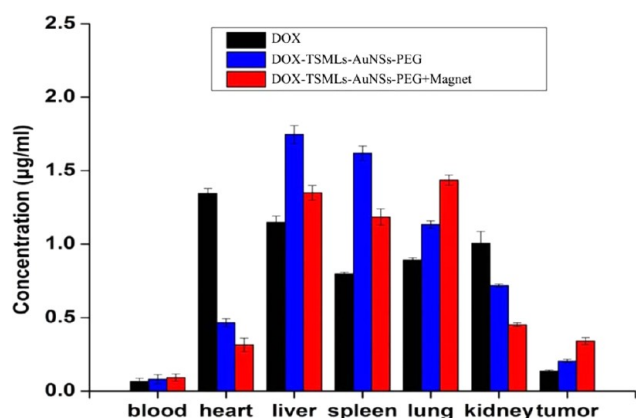

Figure 10. Biodistribution in tumor-bearing mice after 4 h injection (n = 6).

injection for 4 h. The concentrations of DOX in the heart of DOX-TSMLs-AuNSs-PEG, no matter with or without a magnet, were significantly lower than the free DOX group (P < 0.05), indicating that the drug delivery systems can significantly reduce the toxic side effect of free DOX for the heart. In addition, the amount of DOX in a tumor of the DOX-TSMLs-AuNSs-PEG+Magnet group was remarkably higher

than that of DOX-TSMLs-AuNSs-PEG and the free DOX group (P < 0.05). The higher drug delivery efficiency of DOX-TSMLs-AuNSs-PEG+Magnet directly indicates its magnetic tumor targeting efficiency is consistent with the results *in vitro*.

3.8. MR and X-ray Imaging. In this study, MR and X-ray imaging using DOX-TSMLs-AuNSs-PEG were detected *in vitro* above. Whether DOX-TSMLs-AuNSs-PEG could be used for MR and X-ray imaging applications *in vivo*, this delivery system was injected into the tumor-bearing mice model. In Figure 11, as indicated by the red circle, it can be seen that the administration of DOX-TSMLs-AuNSs-PEG enables a clear MR or CT contrast to weaken or enhance the tumor, respectively, demonstrating that this drug delivery system had a great potential in tumor diagnostic applications.

4. CONCLUSION

In summary, a new type of multifunctional drug delivery system (DOX-TSMLs-AuNSs-PEG) was successfully obtained using the high biosafety materials. DOX-TSMLs-AuNSs-PEG can serve not only as a RF-triggered controlled release system but also as a hyperthermia intensifier and a dual-mode MR/X-ray imaging contrast agent. The experiments *in vitro* and *in vivo* showed that DOX-TSMLs-AuNSs-PEG can effectively deliver drugs to the tumor targeted site using its magnetic properties and realize the RF-triggered controlled release. The effective tumor inhibition and dual-mode imaging indicated that there is a great potential of DOX-TSMLs-AuNSs-PEG for simultaneous diagnosis and therapy in biological applications.

■ **AUTHOR INFORMATION**

Corresponding Authors
*Tel.: 86-371-67781910. Fax: 86-371-67781908. E-mail: changjunbiao@zzu.edu.cn.
*E-mail: zhangzz08@126.com.

Notes
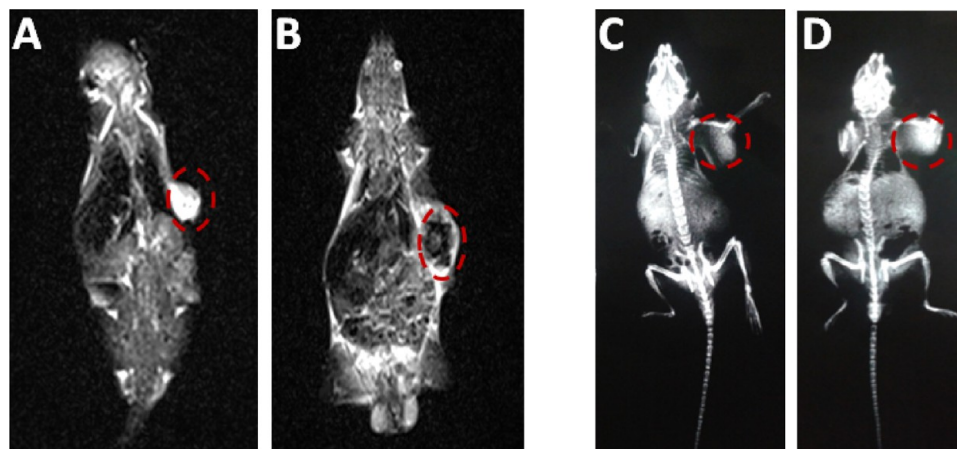The authors declare no competing financial interest.

Figure 11. MR images of (A) control and (B) DOX-TSMLs-AuNSs-PEG *in vivo*. X-ray images of (C) control (31 HU) and (D) DOX-TSMLs-AuNSs-PEG (185 HU) *in vivo* (4 h after injection).

■ REFERENCES

(1) Park, S. M.; Kim, M. S.; Park, S. J.; Park, E. S.; Choi, K. S.; Kim, Y. S.; Kim, H. R. Novel Temperature-Triggered Liposome with High Stability: Formulation, in Vitro Evaluation, and in Vivo Study Combined with High-Intensity Focused Ultrasound (Hifu). *J. Controlled Release* **2013**, *170*, 373−379.

(2) Sato, Y.; Hatakeyama, H.; Sakurai, Y.; Hyodo, M.; Akita, H.; Harashima, H. A Ph-Sensitive Cationic Lipid Facilitates the Delivery of Liposomal Sirna and Gene Silencing Activity in Vitro and in Vivo. *J. Controlled Release* **2012**, *163*, 267−276.

(3) Loew, M.; Forsythe, J. C.; McCarley, R. L. Lipid Nature and Their Influence on Opening of Redox-Active Liposomes. *Langmuir* **2013**, *29*, 6615−6623.

(4) Wang, L.; Shi, J.; Jia, X.; Liu, R.; Wang, H.; Wang, Z.; Li, L.; Zhang, J.; Zhang, C.; Zhang, Z. Nir-/Ph-Responsive Drug Delivery of Functionalized Single-Walled Carbon Nanotubes for Potential Application in Cancer Chemo-Photothermal Therapy. *Pharm. Res.* **2013**, *30*, 2757−2771.

(5) Ratajczak, M. Z.; Jadczyk, T.; Schneider, G.; Kakar, S. S.; Kucia, M. Induction of a Tumor-Metastasis-Receptive Microenvironment as an Unwanted and Underestimated Side Effect of Treatment by Chemotherapy or Radiotherapy. *J. Ovarian Res.* **2013**, *6*, 95.

(6) Wang, C.; Xu, H.; Liang, C.; Liu, Y. M.; Li, Z. W.; Yang, G. B.; Cheng, H.; Li, Y. G.; Liu, Z. Iron Oxide @ Polypyrrole Nanoparticles as a Multifunctional Drug Carrier for Remotely Controlled Cancer Therapy with Synergistic Antitumor Effect. *ACS Nano* **2013**, *7*, 6782−6795.

(7) Ranson, M. R.; Cheeseman, S.; White, S.; Margison, J. Caelyx (Stealth Liposomal Doxorubicin) in the Treatment of Advanced Breast Cancer. *Crit. Rev. Oncol. Hematol.* **2001**, *37*, 115−120.

(8) Rom, J.; Bechstein, S.; Domschke, C.; Golatta, M.; Mayer, C.; Heil, J.; Thum, J.; Smetanay, K.; Windemuth-Kieselbach, C.; Wallwiener, M.; Marme, F.; Schuetz, F.; Sohn, C.; Schneeweiss, A. Efficacy and Toxicity Profile of Pegylated Liposomal Doxorubicin (Caelyx) in Patients with Advanced Breast Cancer. *Anti-Cancer Drugs* **2014**, *25*, 219−224.

(9) Pradhan, P.; Giri, J.; Rieken, F.; Koch, C.; Mykhaylyk, O.; Doblinger, M.; Banerjee, R.; Bahadur, D.; Plank, C. Targeted Temperature Sensitive Magnetic Liposomes for Thermo-Chemo-therapy. *J. Controlled Release* **2010**, *142*, 108−121.

(10) Jiang, S.; Eltoukhy, A. A.; Love, K. T.; Langer, R.; Anderson, D. G. Lipidoid-Coated Iron Oxide Nanoparticles for Efficient DNA and Sirna Delivery. *Nano Lett.* **2013**, *13*, 1059−1064.

(11) Liu, G.; Gao, J.; Ai, H.; Chen, X. Applications and Potential Toxicity of Magnetic Iron Oxide Nanoparticles. *Small* **2013**, *9*, 1533−1545.

(12) Santhosh, P. B.; Ulrih, N. P. Multifunctional Superparamagnetic Iron Oxide Nanoparticles: Promising Tools in Cancer Theranostics. *Cancer Lett.* **2013**, *336*, 8−17.

(13) Bealle, G.; Di Corato, R.; Kolosnjaj-Tabi, J.; Dupuis, V.; Clement, O.; Gazeau, F.; Wilhelm, C.; Menager, C. Ultra Magnetic Liposomes for Mr Imaging, Targeting, and Hyperthermia. *Langmuir* **2012**, *28*, 11843−11851.

(14) Qiu, D.; An, X. Controllable Release from Magnetoliposomes by Magnetic Stimulation and Thermal Stimulation. *Colloids Surf., B* **2013**, *104*, 326−329.

(15) Yan, C. G.; Wu, Y. K.; Feng, J.; Chen, W. F.; Liu, X.; Hao, P.; Yang, R. M.; Zhang, J.; Lin, B. Q.; Xu, Y. K.; Liu, R. Y. Anti-Alpha V Beta 3 Antibody Guided Three-Step Pretargeting Approach Using Magnetoliposomes for Molecular Magnetic Resonance Imaging of Breast Cancer Angiogenesis. *Int. J. Nanomed.* **2013**, *8*, 245−255.

(16) Chiang, W. H.; Huang, W. C.; Chang, C. W.; Shen, M. Y.; Shih, Z. F.; Huang, Y. F.; Lin, S. C.; Chiu, H. C. Functionalized Polymersomes with Outlayered Polyelectrolyte Gels for Potential Tumor-Targeted Delivery of Multimodal Therapies and Mr Imaging. *J. Controlled Release* **2013**, *168*, 280−288.

(17) Mo, R.; Sun, Q.; Li, N.; Zhang, C. Intracellular Delivery and Antitumor Effects of Ph-Sensitive Liposomes Based on Zwitterionic Oligopeptide Lipids. *Biomaterials* **2013**, *34*, 2773−2786.

(18) Koshkaryev, A.; Sawant, R.; Deshpande, M.; Torchilin, V. Immunoconjugates and Long Circulating Systems: Origins, Current State of the Art and Future Directions. *Adv. Drug Delivery Rev.* **2013**, *65*, 24−35.

(19) Lin, C. Y.; Javadi, M.; Belnap, D. M.; Barrow, J. R.; Pitt, W. G. Ultrasound Sensitive Eliposomes Containing Doxorubicin for Drug Targeting Therapy. *Nanomedicine* **2014**, *10*, 67−76.

(20) Tagami, T.; May, J. P.; Ernsting, M. J.; Li, S. D. A Thermosensitive Liposome Prepared with a Cu(2)(+) Gradient Demonstrates Improved Pharmacokinetics, Drug Delivery and Antitumor Efficacy. *J. Controlled Release* **2012**, *161*, 142−149.

(21) Stafford, R. J.; Shetty, A.; Elliott, A. M.; Schwartz, J. A.; Goodrich, G. P.; Hazle, J. D. Mr Temperature Imaging of Nanoshell Mediated Laser Ablation. *Int. J. Hyperthermia* **2011**, *27*, 782−790.

(22) Coughlin, A. J.; Ananta, J. S.; Deng, N.; Larina, I. V.; Decuzzi, P.; West, J. L. Gadolinium-Conjugated Gold Nanoshells for Multimodal Diagnostic Imaging and Photothermal Cancer Therapy. *Small* **2014**, *10*, 556−565.

(23) Tang, H.; Kobayashi, H.; Niidome, Y.; Mori, T.; Katayama, Y.; Niidome, T. Cw/Pulsed Nir Irradiation of Gold Nanorods: Effect on Transdermal Protein Delivery Mediated by Photothermal Ablation. *J. Controlled Release* **2013**, *171*, 178−183.

(24) Shi, P.; Qu, K.; Wang, J.; Li, M.; Ren, J.; Qu, X. Ph-Responsive Nir Enhanced Drug Release from Gold Nanocages Possesses High Potency against Cancer Cells. *Chem. Commun. (Cambridge, U. K.)* **2012**, *48*, 7640−7642.

(25) Sharp, R.; Adams, J.; Machiraju, R.; Lee, R.; Crane, R. Physics-Based Subsurface Visualization of Human Tissue. *IEEE Trans. Vis. Comput. Graph.* **2007**, *13*, 620−629.

(26) Abdo, A.; Sahin, M. Nir Light Penetration Depth in the Rat Peripheral Nerve and Brain Cortex. *Conf. Proc. IEEE Eng. Med. Biol. Soc.* **2007**, *2007*, 1723−1725.

(27) Wang, L.; Shi, J.; Zhang, H.; Li, H.; Gao, Y.; Wang, Z.; Wang, H.; Li, L.; Zhang, C.; Chen, C.; Zhang, Z.; Zhang, Y. Synergistic Anticancer Effect of Rnai and Photothermal Therapy Mediated by Functionalized Single-Walled Carbon Nanotubes. *Biomaterials* **2013**, *34*, 262−274.

(28) Tatli, S.; Tapan, U.; Morrison, P. R.; Silverman, S. G. Radiofrequency Ablation: Technique and Clinical Applications. *Diagn. Interv. Radiol.* **2012**, *18*, 508−516.

(29) Ahmed, M.; Moussa, M.; Goldberg, S. N. Synergy in Cancer Treatment between Liposomal Chemotherapeutics and Thermal Ablation. *Chem. Phys. Lipids* **2012**, *165*, 424−437.

(30) Khan, J. A.; Kudgus, R. A.; Szabolcs, A.; Dutta, S.; Wang, E.; Cao, S.; Curran, G. L.; Shah, V.; Curley, S.; Mukhopadhyay, D.; Robertson, J. D.; Bhattacharya, R.; Mukherjee, P. Designing Nanoconjugates to Effectively Target Pancreatic Cancer Cells in Vitro and in Vivo. *PLoS One* **2011**, *6*, e20347.

(31) Moran, C. H.; Wainerdi, S. M.; Cherukuri, T. K.; Kittrell, C.; Wiley, B. J.; Nicholas, N. W.; Curley, S. A.; Kanzius, J. S.; Cherukuri, P. Size-Dependent Joule Heating of Gold Nanoparticles Using Capacitively Coupled Radiofrequency Fields. *Nano Res.* **2009**, *2*, 400−405.

(32) Selbo, P. K.; Weyergang, A.; Hogset, A.; Norum, O. J.; Berstad, M. B.; Vikdal, M.; Berg, K. Photochemical Internalization Provides Time- and Space-Controlled Endolysosomal Escape of Therapeutic Molecules. *J. Controlled Release* **2010**, *148*, 2−12.

(33) Qin, Z. P.; Bischof, J. C. Thermophysical and Biological Responses of Gold Nanoparticle Laser Heating. *Chem. Soc. Rev.* **2012**, *41*, 1191−1217.

(34) Kim, H.; Lee, D.; Kim, J.; Kim, T. I.; Kim, W. J. Photothermally Triggered Cytosolic Drug Delivery Via Endosome Disruption Using a Functionalized Reduced Graphene Oxide. *ACS Nano* **2013**, *7*, 6735−6746.

(35) Khan, F. R.; Kennaway, G. M.; Croteau, M. N.; Dybowska, A.; Smith, B. D.; Nogueira, A. J. A.; Rainbow, P. S.; Luoma, S. N.; Valsami-Jones, E. In Vivo Retention of Ingested Au Nps by Daphnia Magna: No Evidence for Trans-Epithelial Alimentary Uptake. *Chemosphere* **2014**, *100*, 97−104.

(36) Kiwada, H.; Sato, J.; Yamada, S.; Kato, Y. Feasibility of Magnetic Liposomes as a Targeting Device for Drugs. *Chem. Pharm. Bull.* **1986**, *34*, 4253−4258.

(37) Wang, T.; Zhang, L.; Wang, H.; Yang, W.; Fu, Y.; Zhou, W.; Yu, W.; Xiang, K.; Su, Z.; Dai, S.; Chai, L. Controllable Synthesis of Hierarchical Porous Fe3o4 Particles Mediated by Poly-(Diallyldimethylammonium Chloride) and Their Application in Arsenic Removal. *ACS Appl. Mater. Interfaces* **2013**, *5*, 12449−12459.

(38) Zhu, H.; Du, M. L.; Zou, M. L.; Xu, C. S.; Li, N.; Fu, Y. Q. Facile and Green Synthesis of Well-Dispersed Au Nanoparticles in Pan Nanofibers by Tea Polyphenols. *J. Mater. Chem.* **2012**, *22*, 9301−9307.

(39) Li, J. C.; Zheng, L. F.; Cai, H. D.; Sun, W. J.; Shen, M. W.; Zhang, G. X.; Shi, X. Y. Facile One-Pot Synthesis of Fe3o4@Au Composite Nanoparticles for Dual-Mode Mr/Ct Imaging Applications. *ACS Appl. Mater. Interfaces* **2013**, *5*, 10357−10366.

(40) Noda, M.; Shimanouchi, T.; Okuyama, M.; Kuboi, R. A Bio-Thermochemical Microbolometer with Immobilized Intact Liposome on Sensor Solid Surface. *Sensors Actuators, B-Chem.* **2008**, *135*, 40−45.

(41) Fazal, S.; Jayasree, A.; Sasidharan, S.; Koyakutty, M.; Nair, S. V.; Menon, D. Green Synthesis of Anisotropic Gold Nanoparticles for Photothermal Therapy of Cancer. *ACS Appl. Mater. Interfaces* **2014**, *6*, 8080−8089.

(42) Li, J.; Zheng, L.; Cai, H.; Sun, W.; Shen, M.; Zhang, G.; Shi, X. Facile One-Pot Synthesis of Fe3o4@Au Composite Nanoparticles for Dual-Mode Mr/Ct Imaging Applications. *ACS Appl. Mater. Interfaces* **2013**, *5*, 10357−10366.

(43) Zhou, Z.; Zhang, C.; Qian, Q.; Ma, J.; Huang, P.; Zhang, X.; Pan, L.; Gao, G.; Fu, H.; Fu, S.; Song, H.; Zhi, X.; Ni, J.; Cui, D., Folic Acid-Conjugated Silica Capped Gold Nanoclusters for Targeted Fluorescence/X-Ray Computed Tomography Imaging. *J. Nano-biotechnol.* **2013**, *11*.

(44) Stacy, B. M.; Comfort, K. K.; Comfort, D. A.; Hussain, S. M. In Vitro Identification of Gold Nanorods through Hyperspectral Imaging. *Plasmonics* **2013**, *8*, 1235−1240.

(45) Sheihet, L.; Garbuzenko, O. B.; Bushman, J.; Gounder, M. K.; Minko, T.; Kohn, J. Paclitaxel in Tyrosine-Derived Nanospheres as a Potential Anti-Cancer Agent: In Vivo Evaluation of Toxicity and Efficacy in Comparison with Paclitaxel in Cremophor. *Eur. J. Pharm. Sci.* **2012**, *45*, 320−329.

(46) Synold, T. W.; Xi, B. X.; Wu, J.; Yen, Y.; Li, B. C.; Yang, F.; Phillips, J. W.; Nickols, N. G.; Dervan, P. B. Single-Dose Pharmacokinetic and Toxicity Analysis of Pyrrole-Imidazole Poly-amides in Mice. *Cancer Chemother. Pharmacol.* **2012**, *70*, 617−625.